PAPER

# A Capacitance Varying Charge Pump with Exponential Stage-Number Dependence and Its Implementation by MEMS Technology

**Menghan SONG**[†a)], *Nonmember and* **Tamio IKEHASHI**[†b)], *Member*

**SUMMARY** A novel charge pump, Capacitance Varying Charge Pump (CVCP) is proposed. This charge pump is composed of variable capacitors and rectifiers, and the charge transfer is attained by changing the capacitance values in a manner similar to peristaltic pumps. The analysis of multi-stage CVCP reveals that the output voltage is exponentially dependent on the stage number. Thus, compared with the Dickson charge pump, this charge pump has an advantage in generating high voltages with small stages. As a practical example of CVCP, we present an implementation realized by a MEMS (Micro-Electro-Mechanical Systems) technology. Here, the variable capacitor is enabled by a comb-capacitor attached to a high-quality factor resonator. As the rectifier, a PN-junction diode formed in the MEMS layer is used. Simulations including the mechanical elements are carried out for this MEMS version of CVCP. The simulation results on the output voltage and load characteristics are shown to coincide well with the theoretical estimations. The MEMS CVCP is suited for MEMS devices and vibration energy harvesters.

***key words:*** *charge pump, MEMS, comb-capacitor, resonator, diode*

## 1. Introduction

Charge pumps are the circuits that generate a higher voltage than the supply voltage. They are used extensively in systems where a high voltage is required, such as nonvolatile memories [1], LCD drivers [2], energy harvesting systems [3]–[5] and MEMS applications [6], [7], including MEMS actuators [8] and gyroscopes [9].

The Dickson charge pump (DCP) and its variants are the most widely used charge pump [10]. This charge pump is composed of capacitors and CMOS-based rectifiers. A high voltage can be produced by supplying voltage pulses to the capacitors and thereby transferring the stored charge to the output. To date, many variations of DCP are proposed to enhance the performance of the charge pump [11]–[16].

In this paper, we present a novel charge pump which we call a Capacitance Varying Charge Pump (CVCP). In this charge pump, capacitance change of variable capacitors enables the charge transfer. We prove that the output voltage of this charge pump is exponentially dependent on the stage number, in contrast to DCP's linear stage number dependence. This paper aims to reveal the basic properties of CVCP, including the maximum output voltage and load characteristics. The theoretical results are verified by simulations.

In principle, CVCP may be realized in many ways. The only required constituents are variable capacitors and rectifiers. But here, to demonstrate and analyze the CVCP performance in detail, we examine a MEMS version of CVCP. In this implementation, a MEMS comb capacitor is adopted for the variable capacitor and a diode formed in the MEMS layer serves as the rectifier. The capacitance change is achieved by attaching one end of the capacitor to a MEMS resonator. If a high-quality factor (high-$Q$) MEMS resonator is employed, a large amplitude can be attained with low power. This enables large capacitance change and higher charge transfer efficiency.

The formation of CVCP requires special fabrication process and package, as can be understood from the above. Thus, CVCP is not a charge pump that can be used in place of conventional DCPs. Especially, it is not suited for CMOS LSI. However, the MEMS CVCP is useful for System-in-Package (SIP) type MEMS devices that call for high actuation voltages [17]. In this kind of module, a high voltage generated in the CMOS chip needs to be supplied to the MEMS chip via interconnects. This, however, induces deterioration of the charge pump efficiency owing to the large parasitic capacitances. A CVCP formed in the MEMS layer can avoid this issue. Also, this CVCP does not require high-voltage tolerant MOSFETs. This can reduce the CMOS chip cost.

MEMS CVCP is not the only way to generate a high voltage in the MEMS layer. For example, a charge pump controlled by micromechanical resonant switches has been proposed [18]. However, the mechanical contact switch used in this approach can have a reliability issue. In this respect, CVCP is advantageous as it does not require physical contact.

The MEMS CVCP is especially suited for MEMS devices that possess resonators, since mechanical elements of CVCP, i.e., resonators and variable capacitors, can be constructed by the same fabrication process. Examples that belong to this class are MEMS gyros [19] and silicon oscillators [2]. MEMS CVCP can also be used for a charge pump that generates a supply voltage in vibration energy harvesting systems.

This paper is organized as follows. Section 2 presents the basic concepts and operating principles of a single-stage CVCP. The composition of the CVCP is compared with

Manuscript received May 8, 2023.
Manuscript publicized June 26, 2023.
[†]The authors are with the University of Waseda IPS, Kitakyushu-shi, 808–0135 Japan.
a) E-mail: song_menghan@akane.waseda.jp
b) E-mail: t.ikehashi@waseda.jp
DOI: 10.1587/transele.2023ECP5019

a conventional Dickson charge pump. Section 3 explains multi-stage CVCPs. Here, the performance of an $N$-stage CVCP is theoretically analyzed, and expressions of the output voltage and effective resistance are derived. In Sect. 4, a MEMS structure that realizes CVCP is discussed. A three-stage FEM model and relevant simulation results are presented and compared with the analytical predictions. Energy consumption analysis is discussed in Sect. 5. The conclusion of the paper will be given at the end.

## 2. Operating Principle of CVCP

### 2.1 Comparison with DCP and CVCP

It is instructive to compare our CVCP with the conventional DCP. Schematics of DCP and CVCP are illustrated in Fig. 1. As the rectifiers, diodes, or diode-connected FETs can be used.

In DCP, the charge transfer is attained by supplying complementary clock pulses to the capacitors. Due to the rectifier, the charge will be transferred in a unidirectional manner. And the amount of the charge transfer, determined by the clock pulse amplitude $V_{CLK}$, is the same for every stage. Thus, the output voltage of DCP will become proportional to the stage number $N$. If a diode-connected MOSFET with a threshold $V_{th}$ is employed as the rectifier, the output voltage of $N$-stage DCP for a supply voltage $V_{DD}$ is given by [11]

$$V_{out-DCP} = V_{DD} - V_{th} + N(V_{CLK} - V_{th}). \tag{1}$$

Therefore, the number of stages is determined by the amplitude $V_{CLK}$, which is usually equal to $V_{DD}$. The threshold voltage $V_{th}$ can be reduced, for example, by 4-phase charge transfer methods [12], [13].

In CVCP, variable capacitors are attached to the nodes between the rectifiers, as shown in Fig. 1 (b). The other nodes of the capacitors are connected to the ground. When the rectifiers are turned off, the $i$-th node charge $Q_i = C_i V_i$ is conserved. Thus, the voltage $V_i$ can be changed by changing the capacitance value $C_i$. And when the voltage $V_i$ becomes large enough, a part of the charge $Q_i$ will be transferred to the next stage through the rectifier. This is the basic operating principle of CVCP.

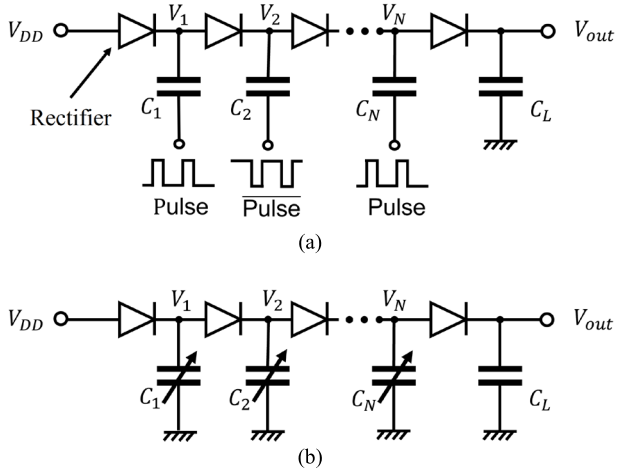


**Fig. 1** Schematic of (a) $N$-stage Dickson charge pump (DCP), (b) $N$-stage capacitance varying charge pump (CVCP).

This circuit is essentially different from the reported charge pumps that show exponential stage number dependence [21]–[23]. As shown in Fig. 2, the output of each stage is fed as the input to the subsequent stage, controlled by switches with two complementary clock phases. The ideal output voltage of an $N$-stage exponential charge pump is $2^N V_{DD}$. In reality, however, it is not easy to transfer the voltage without a voltage drop in the switches. Also, the additional parasitic capacitance deteriorates the charge transfer efficiency. In contrast to this, our CVCP does not require this kind of switch device.

### 2.2 Single-Stage CVCP

To better understand the concept and operation of CVCP, let's first consider a single-stage case shown in Fig. 3. The variable capacitor can be realized by a MEMS structure, and one end of the capacitor is attached to a mass of a spring-mass-damper system. Thus, the capacitance value $C(x)$ is determined by the position $x$ of the movable mass. The spring-mass-damper resonator is driven by an external force $F_{drive}$ at its resonance frequency.

A quality factor $Q$ of a resonator is expressed as $Q = 2\pi E_{stored}/E_{dissipated}$, where $E_{stored}$ is energy stored in the resonator and $E_{dissipated}$ is energy dissipated per cycle. In MEMS resonators, the main cause of energy dissipation is air damping. The air damping can be reduced if the resonator is embedded in a vacuum package, and a quality factor as high as $100k$ can be achieved [24]–[27]. This implies that energy

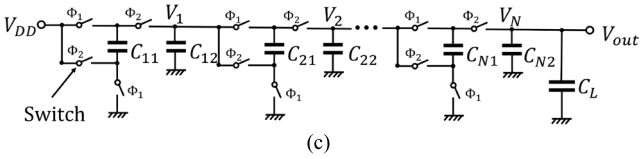


**Fig. 2** Schematic of $N$-stage exponential charge pump.

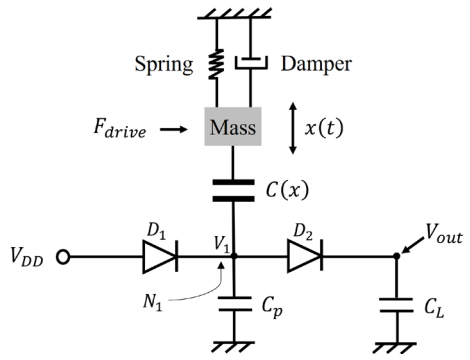


**Fig. 3** Conceptual diagram of single-stage CVCP. $C_p$ is parasitic capacitance. $C_L$ is load capacitance.

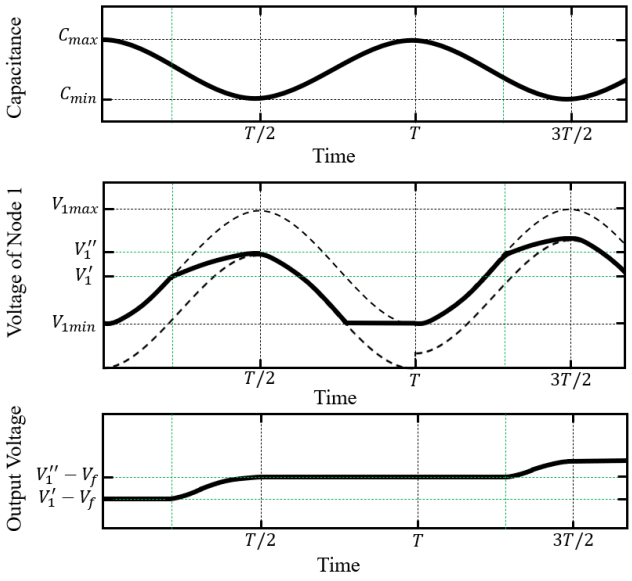


**Fig. 4** The waveform of capacitance $C(x)$, the voltage of node $N_1$ and output voltage $V_{out}$.

supplied from the external force can be reduced drastically for high-$Q$ resonators.

In this charge pump, the vibration of the resonator makes the capacitance change, and this enables the charge transfer. In this sense, a part of the vibration energy is used for the charge transfer. This means that if the external force $F_{drive}$ is not applied, the resonator amplitude will decrease during the charge pumping. The amount of amplitude decrease is determined by the amount of electrical energy transferred to the output. As discussed in Sect. 5, the mechanical vibration energy is usually larger than the electrical energy for typical MEMS resonators. This suggests that if the initial mechanical energy is large enough, the charge pumping to a fixed load capacitance can be finished without significant amplitude decrease.

Now, let's examine the operation of this charge pump based on Fig. 4. We assume that sinusoidal capacitance change is achieved between $C_{min}$ and $C_{max}$, which are the minimum and maximum capacitance values, respectively. The parasitic capacitance of node $N_1$ is $C_p$, and the load capacitance is $C_L$. In the beginning, the voltages $V_1$ and $V_{out}$ are pre-charged to $V_{DD} - V_f$ via the diodes. When the capacitance value decreases from $C_{max}$, $V_1$ starts to increase due to the charge conservation. When the diode $D_2$ turns on at the voltage $V_1'$, part of the charge at node $N_1$ is shared with the output node, and $V_{out}$ start to increase. But since there exists a diode $D_2$, the voltage difference between $V_1$ and $V_{out}$ remains at $V_f$. The diode $D_2$ turns off when the capacitance value reaches $C_{min}$ and after that, $V_1$ will decrease. When $V_1$ becomes lower than $V_{DD} - V_f$, charge will be supplied from $V_{DD}$.

If this procedure is repeated many times, the output voltage will finally reach a value at which no charge is transferred from $N_1$. In this case, the maximum voltage $V_{1max}$ of $N_1$ is obtained from the charge conservation between $C_{min}$ and $C_{min}$ state,

$$(C_{min} + C_p)V_{1max} = (C_{max} + C_p)(V_{DD} - V_f). \tag{2}$$

From this, the maximum output voltage $V_{out\_max}$ is obtained as

$$V_{out\_max} = V_{1max} - V_f = A(V_{DD} - V_f) - V_f, \tag{3}$$

where

$$A = \frac{C_{max} + C_p}{C_{min} + C_p} \tag{4}$$

is a gain of the charge pump, $C_p$ is parasitic capacitance.

In the above formulation, the parasitic capacitance of the rectifier is neglected. Let's now include this effect. If PN-junction diodes are used as the rectifiers, the junction capacitance value should depend on the applied voltage. In this paper, to simplify the analysis, we assume that the junction capacitance value is constant, and use the value of zero-bias junction capacitance $C_{j0}$. Then $A$ of Eq. (4) is modified to

$$A = \frac{C_{max} + C_p + 2C_{j0}}{C_{min} + C_p + 2C_{j0}}. \tag{5}$$

This result suggests that the output voltage of CVCP can be increased for the larger gain $A$. This is attained at larger $C_{max}$, smaller $C_{min}$, smaller $C_p$, and smaller $C_{j0}$.

An example of a variable capacitor that can attain a large gain $A$ is depicted in Fig. 5. This is a comb-capacitor realized in MEMS technology. Here, the gap $g_1$ is the gap of as-fabricated state. This value is determined by the process rules. The maximum capacitance state is achieved when the electrode overlap area becomes maximum. The gap $g_2$ in this state can be made smaller than the gap $g_1$, thanks to the movable nature of MEMS structure. On the other hand, $C_{min}$ can be made very small since there are no overlaps and the two structures are far apart. Therefore, we can attain a high capacitance ratio $C_{max}/C_{min}$. This enables large gain $A$.

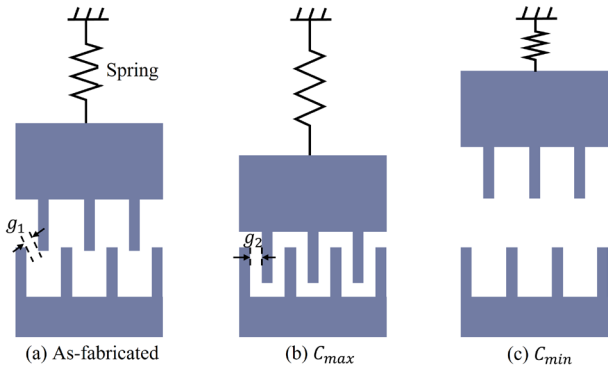


**Fig. 5** An example of variable capacitor employed in CVCP. (a) is as-fabricated capacitor state, (b) is the state with maximum capacitance $C_{max}$, and (c) is the state with minimum capacitance $C_{min}$. The comb electrode configuration with $g_1 > g_2$ enables large capacitance ratio $C_{max}/C_{min}$.

## 3. Multi-Stage CVCP

### 3.1 Concept and Operation of Multi-Stage CVCP

To generate a higher voltage in CVCP, a multi-stage configuration as shown in Fig. 1 should be used. We assume that all variable capacitors have the same maximum and minimum capacitance values. We denote them as $C_{max}$ and $C_{min}$, respectively. Now let's consider $i$-th and $i+1$ -th stage of the multi-stage CVCP, as shown in Fig. 6. If we assume that the rectifier is turned off, the voltage difference $V_i - V_{i+1}$ will become maximum when $C_i$ is $C_{min}$ and $C_{i+1}$ is $C_{max}$. This suggests that the transferred charge $\Delta q$ through the rectifier can be maximized when the two variable capacitors are driven in an anti-phase fashion. Thus, the charge-transfer efficiency of the whole CVCP can be maximized when the even and odd variable capacitors are driven in anti-phase, or with a phase difference of $\pi$. This situation is illustrated in Fig. 7. The anti-phase drive of CVCP corresponds to the complementary pulsing of even and odd stages in the case of DCP.

We would like to point out that the operation of CVCP shown in Fig. 7 resembles a peristaltic pump used for fluids [28], [29]. In peristaltic pumps, fluids are transported by expanding and shrinking a volume, as in the peristalsis of living organisms. In CVCP, the volume change is replaced by the capacitance change.

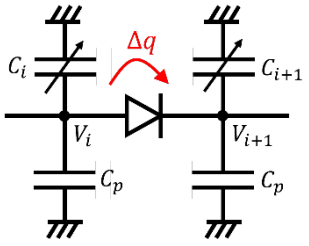


**Fig. 6** Stage $i$ and $i+1$ of the multi-stage CVCP. Here, $C_i$, $C_{i+1}$ are variable capacitances and $C_p$ is parasitic capacitance.

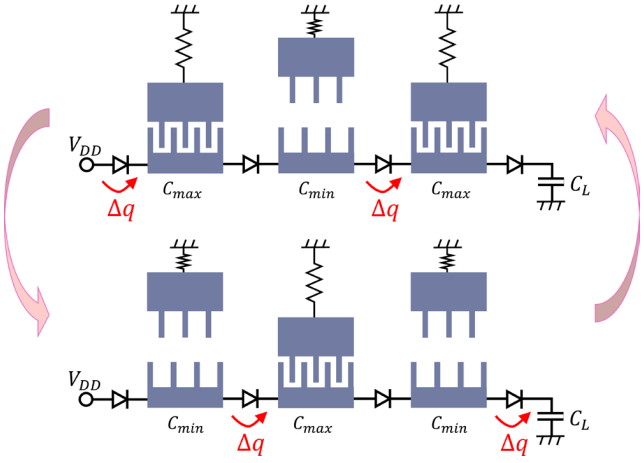


**Fig. 7** Multi-stage charge pump operation. Charge transfer $\Delta q$ is attained by anti-phase drive of even and odd stages. This operating principle is similar to peristaltic pumps.

To show the behavior of the variable capacitor more explicitly, let's consider a case when the capacitance $C_i$ is determined by a position $x$ given by

$$x = x_0 \cos(2\pi f t), \tag{6}$$

where $x_0$ is the amplitude and $f$ is the frequency. For simplicity, let's assume that $C_i$ is proportional to this position $x$. The time dependence of the capacitances is then written as:
$i$ = odd:

$$C_i = \frac{1}{2}\{(C_{max} - C_{min})\cos(2\pi f t) + C_{max} + C_{min}\}, \tag{7}$$

$i$ = even:

$$C_i = \frac{1}{2}\{(C_{max} - C_{min})\cos(2\pi f t + \pi) + C_{max} + C_{min}\}. \tag{8}$$

The capacitance and voltage waveforms of stage $i$ and $i+1$ are illustrated in Fig. 8. As shown in the figure, CVCP operation for a cycle time $T(= 1/f)$ can be divided into four phases. The states of rectifiers corresponding to the four phases are schematically shown in Fig. 9. During phase 1, the rectifiers $D_i$ and $D_{i+1}$ are both turned off. In this case, the voltage $V_i$ increases as the capacitance $C_i$ decreases. Phase 2 starts when the voltage difference $V_i - V_{i+1}$ becomes $V_f$. Since the rectifier $D_{i+1}$ turns on, the charge will be transferred from stage $i$ to $i+1$ based on charge sharing. After that, $C_i$ becomes $C_{min}$, and enters phase 3. Here, $D_i$ and $D_{i+1}$ will be turned off again. The voltage $V_i$ decreases while $C_i$ increases, and when $D_i$ turns on, it goes into phase 4. During phase 4, charge will be supplied from the previous stage $i-1$.

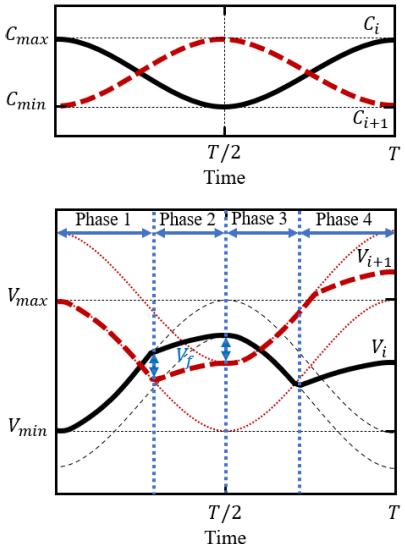


**Fig. 8** Waveform of multi-stage capacitance $C_i$ and $C_{i+1}$, voltage of node $V_i$ and $V_{i+1}$.

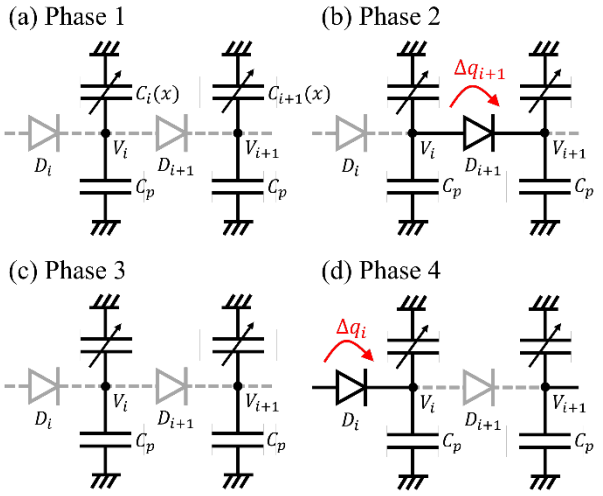


**Fig. 9** States of rectifiers for (a) phase 1, (b) phase 2, (c) phase3, and (d) phase 4. Grey/dashed portions represent off states of the rectifier and $C_p$ is the parasitic capacitance.

### 3.2 Output Voltage of $N$-Stage CVCP in Steady State

Dynamical analysis of CVCP, i.e., theoretical analysis while the output voltage is changing, is not easy. But we can still find a steady state solution in which the charge transferred to the output per cycle is constant. If we denote this charge as $q$, then the charge transferred from stage $i-1$ to $i$ and that from stage $i$ to $i+1$ also becomes $q$. Therefore, we get an equation

$$(C_{max} + C_p + 2C_{j0})v_i' - (C_{min} + C_p + 2C_{j0})v_i = q, \quad (9)$$

where $v_i'$ and $v_i$ are voltages of stage $i$ when the capacitance $C_i$ is $C_{max}$ and $C_{min}$, respectively. As before, we assumed constant capacitance $C_{j0}$ for the diode junction capacitance. When the total stage number is $N$, the equation (9) holds for $i = 1, \cdots, N$. Note that while $v_i$ corresponds to the maximum voltage of the stage $i$, $v_i'$ does not necessarily correspond to the minimum voltage, as suggested from Fig. 8. Also, from phase 2 of Fig. 8, an identity below holds at $C_i = C_{min}$:

$$v_{i+1}' = v_i - V_f. \quad (10)$$

If we eliminate $v_i'$ using (9) and (10), we obtain a recurrence formula for $v_i$:

$$v_i = A(v_{i-1} - V_f) - \frac{q}{C_{min} + C_p + 2C_{j0}} \quad (11)$$

with $i = 2, \cdots, N$. For $i = 1$, we can use this equation with $v_0$ replaced by $V_{DD}$:

$$v_1 = A(V_{DD} - V_f) - \frac{q}{C_{min} + C_p + 2C_{j0}}. \quad (12)$$

The recurrence formula (11) can be solved in the standard way. Namely, we first recast the equation in the form

$$v_i - B = A(v_{i-1} - B), \quad (13)$$

where

$$B \equiv \frac{1}{A-1}\left(AV_f + \frac{q}{C_{min} + C_p + 2C_{j0}}\right). \quad (14)$$

Then we can solve the equation in an iterative manner:

$$\begin{aligned} v_N - B &= A(v_{N-1} - B) \\ &= \cdots \\ &= A^{N-1}(v_1 - B). \end{aligned} \quad (15)$$

Since a rectifier is inserted between the stage $N$ and the output, the relationship between $v_N$ and the output voltage $V_{out}$ is

$$V_{out} = v_N - V_f. \quad (16)$$

Inserting (12) and (16) into (15), we obtain the expression of $V_{out}$ for $N$ stage case:

$$V_{out} = A^N V_{DD} - \frac{A^{N+1} - 1}{A-1}V_f - \frac{A^N - 1}{A-1}\frac{q}{C_{min} + C_p + 2C_{j0}}. \quad (17)$$

The charge $q$ can be written in terms of the output current $I_{out}$ and the cycle time $T$ as

$$q = I_{out}T. \quad (18)$$

Using this, the equation (17) can be expressed in the form of load characteristics:

$$V_{out} = V_{max} - R_{eff}I_{out}, \quad (19)$$

where

$$V_{max} = A^N V_{DD} - \frac{A^{N+1} - 1}{A-1}V_f \quad (20)$$

is the maximum output voltage and

$$R_{eff} = \frac{A^N - 1}{A-1}\frac{T}{C_{min} + C_p + 2C_{j0}} \quad (21)$$

is the effective resistance of the charge pump.

To interpret this result of CVCP, let's compare this load characteristics with that of DCP. The maximum voltage and the effective resistance for a steady state $N$-stage DCP are given by [11]

$$V_{max}[DCP] = (N+1)(V_{DD} - V_{th}), \quad (22)$$

$$R_{eff}[DCP] = \frac{NT}{C}, \quad (23)$$

where $C$ is a capacitance value of unit stage.

If we compare the two expressions, we can see that while $V_{max}$ is linearly dependent on $N$ for DCP, it is exponentially dependent on $N$ for CVCP. Thus, CVCP has an advantage in generating a high voltage with relatively small stage numbers. This result is stemming from the anti-phase

**Table 1** Comparison with DCP.

| | DCP [10] | CVCP |
|---|---|---|
| $V_{max}$ | $(N+1)(V_{DD}-V_{th})$ | $A^N V_{DD} - \frac{A^{N+1}-1}{A-1}V_f$ |
| $R_{eff}$ | $\frac{NT}{C}$ | $\frac{A^N-1}{A-1}\frac{T}{C_{min}+C_p+2C_{j0}}$ |
| $Frequency$ | $> 10MHz$ | $< 100kHz$ |

capacitance drive method that enables efficient charge transfer. The same exponential $N$ dependence is attained for the effective resistance. However, in contrast to DCP that shows smaller $R_{eff}$ for larger $C$, $R_{eff}$ of CVCP becomes larger for larger gain $A$ and hence larger $C_{max}$. Current supplying capability of CVCP is thus weaker for larger $A$ and $N$. This is a side effect of the high voltage generating capability. These properties should be noticed when designing the CVCP system. The main differences between DCP and CVCP are summarized in Table 1.

## 4. Simulations Results and Discussion

### 4.1 Three-Stage CVCP System

Up to here, we discussed the theoretical properties of CVCP. These properties can, in principle, be achieved by versatile technologies. From now on, we will discuss more practical implementation using MEMS technology. We also try to reproduce the theoretical results using simulations.

As the variable capacitor, we employ a MEMS comb-capacitor structure shown in Fig. 5. As we have seen in Fig. 8, when the even and odd stage capacitors are driven in anti-phase fashion, they exhibit the highest voltage difference in one cycle, resulting in the largest transfer charge $\Delta q$. Here, the anti-phase drive means that the even stage capacitances should become maximum when the odd stage capacitances become minimum, and vise versa. Simplest way to realize this situation is to attach even and odd stage variable capacitors to opposite sides of a single movable structure. An example of a three-stage CVCP that realizes this condition is shown in Fig. 10. Here, $C_1$, $C_2$ and $C_3$ are the variable capacitors. When the capacitance $C_1$ and $C_3$ becomes maximum, $C_2$ becomes minimum and vice versa. In this way, the anti-phase operation can be attained naturally.

The vibrational motion of the resonator is achieved by applying an AC voltage to the actuator. To maximize the capacitance change $C_{max} - C_{min}$ and hence the gain $A$, the resonator must be actuated at its resonance frequency determined by the mass and spring constant. This is achieved by monitoring the amplitude by the sensor electrode and tuning the frequency using a closed-loop feedback [24], [30]. Circuits that attain this function is well-known and the details will not be discussed here. Note that the overlap between the electrodes should always exist for the actuators and sensors,

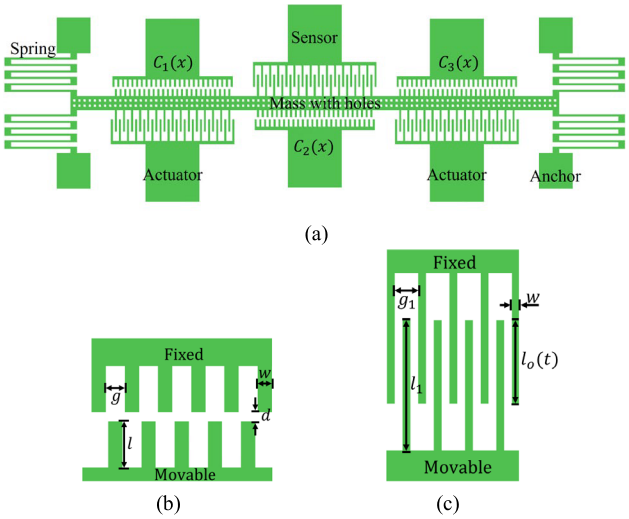


**Fig. 10** Mechanical structure of (a) a three-stage CVCP, (b) comb-capacitor, (c) sensor and actuator.

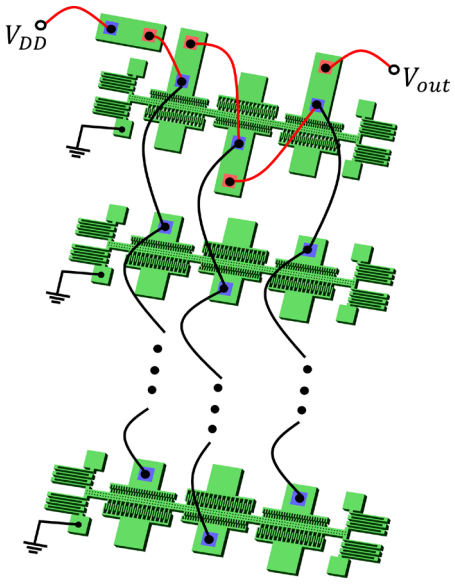


**Fig. 11** Electrical configuration of three-stage CVCP. The parallel connection of ten identical structures is used to increase the capacitance. PN junction diodes are placed between the blue and red colored terminals. The interconnections can be done using a cap structure [19], [31].

in contrast to the variable capacitors.

Due to the limited amplification capability of a single comb-capacitor, we achieve a higher capacitance ratio $C_{max}/C_{min}$ by connecting ten capacitors in parallel, as illustrated in Fig. 11. As the rectifiers, PN-junction diodes formed on the MEMS layer are used. Isolation of diodes can be attained by Deep-RIE trenches. Electrical connections between the adjacent capacitors can be done using a cap structure as in references [31], [32].

To carry out simulations, we assume mechanical parameters as summarized in Table 2. The thickness of the silicon layer is assumed to be $30\mu m$ with a minimum line/space of

**Table 2** Mechanical structure dimensions.

| Parameters | Value | Units |
|---|---|---|
| Capacitor electrode width, $w$ | 3.00 | $\mu m$ |
| Capacitor electrode length, $l$ | 10.0 | $\mu m$ |
| Initial distance of capacitor electrode, $d$ | 3.00 | $\mu m$ |
| Gap of capacitor electrode, $g$ | 4.00 | $\mu m$ |
| Capacitor finger number | 25.0 | - |
| Sensor and actuator electrode width, $w$ | 3.00 | $\mu m$ |
| Sensor and actuator electrode length, $l_1$ | 30.0 | $\mu m$ |
| Initial overlap of sensor and actuator, $l_o$ | 18.0 | $\mu m$ |
| Gap of sensor and actuator electrode, $g_1$ | 9.00 | $\mu m$ |
| Sensor finger number | 15.0 | - |
| Actuator finger number | 15.0 | - |
| Mass width | 724 | $\mu m$ |
| Mass length | 19.5 | $\mu m$ |
| Hole width | 3.00 | $\mu m$ |
| Hole length | 3.00 | $\mu m$ |
| Si layer thickness | 30.0 | $\mu m$ |
| Si layer width | 960 | $\mu m$ |
| Si layer length with PN junction diodes | 475 | $\mu m$ |
| Si layer length without PN junction diodes | 275 | $\mu m$ |
| Si mass | 1.53 | $nKg$ |
| Effective spring constant, $k_{eff}$ | 97.8 | $N/m$ |
| Resonance frequency | 40.2 | $kHz$ |

$3\mu m$. This structure can be fabricated by applying Deep-RIE to a Silicon-on-Glass (SOG) wafer [33]. The use of SOG is advantageous in minimizing the parasitic capacitances [32], [34]. The circuit area is estimated based on parameters shown in Table 2 and the result is found to be $4.2mm^2$.

### 4.2 Simulation Results

Mechanical simulation of the resonator part is carried out using Coventor's multi-physics simulation tool $MEMS+^{®}$. The simulated capacitance $C_i(i = 1, 2, 3)$ as a function of the mass position is plotted in Fig. 12. The capacitance value increases linearly as the electrodes start to overlap. When the overlap disappears, the capacitance value seems to keep a constant value according to Fig. 12 (a). However, a slight position dependence due to the fringe capacitances can be observed if that portion is magnified as in Fig. 12 (b).

Total capacitances are found to be $C_{min} = 419fF$ and $C_{max} = 2.44pF$ when the resonator amplitude is $10\mu m$. The capacitance ratio $C_{max}/C_{min}$ can be increased by employing a larger amplitude. But this can bring about nonlinearity in the amplitude-frequency characteristics. In this study, we choose $10\mu m$ amplitude and $40.2kHz$ resonance frequency.

The simulation of the PN-junction diode is performed using Synopsys' Sentaurus® TCAD, and its performance result is shown in Fig. 13. Due to the relatively low total current in our system, the forward voltage of the diode is approximately $0.32V$. The zero-bias junction capacitance $C_{j0}$ is found to be $0.21pF$.

The simulation of this charge pump system is carried out based on Simulink® and Simscape™ of MATLAB®. The mechanical resonator is represented by a spring-mass-damper system described by Simulink®. An external drive force is applied to compensate the energy loss induced by the damping and to keep the $10\mu m$ amplitude. The resonator mass position is reflected in the variable capacitance value.

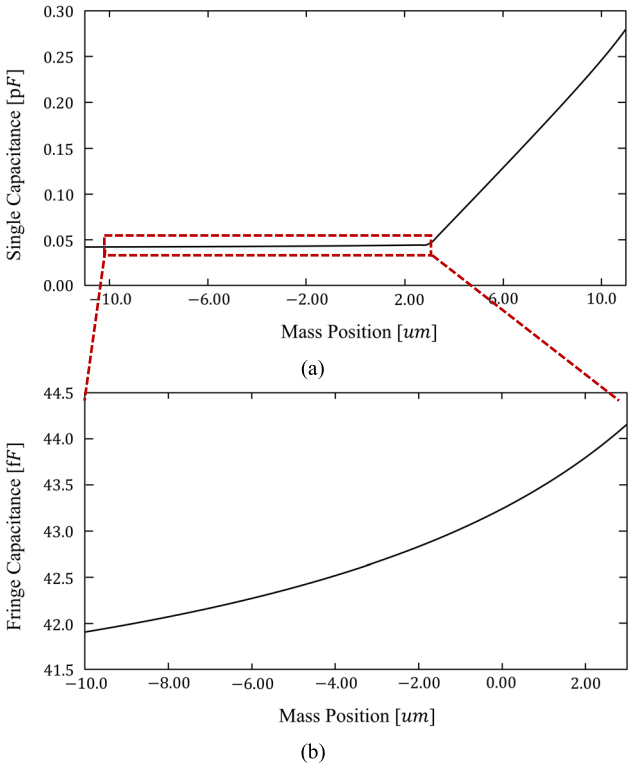


**Fig. 12** Simulation results of (a) single capacitance, (b) fringe capacitance.

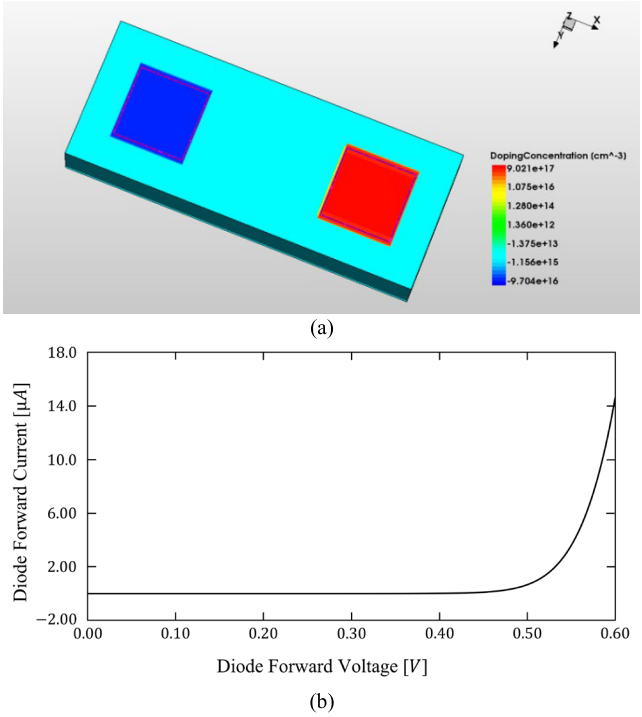


**Fig. 13** Sentaurus® TCAD simulation results of (a) PN-junction diode, (b) I-V characteristic curve.

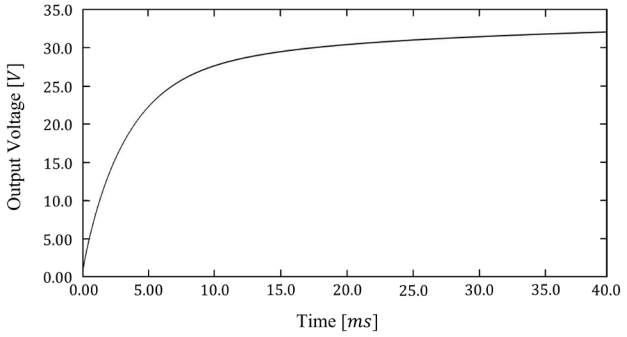


**Fig. 14** Simulation result of $10\mu m$ amplitude three-stage charge pumping operation, with $C_L = 10pF$, $C_p = 0.20pF$ and $C_{j0} = 0.21pF$.

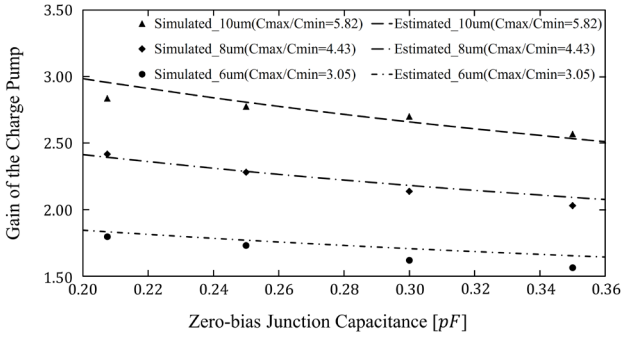


**Fig. 15** Gain of the charge pump dependence on the zero-bias junction capacitance, with $C_L = 10pF$, and $C_p = 0.20pF$.

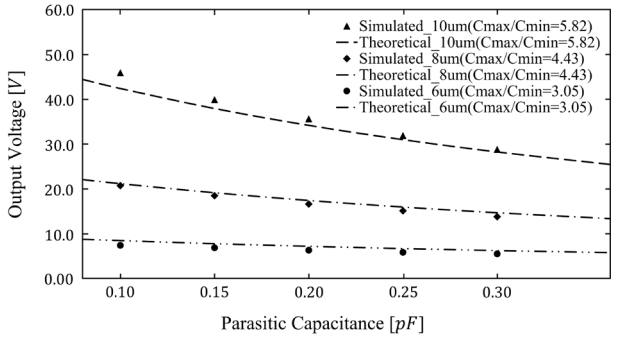


**Fig. 16** Parasitic capacitance dependence of the three-stage CVCP output voltage, with $C_L = 10pF$, and $C_j0 = 0.21pF$.

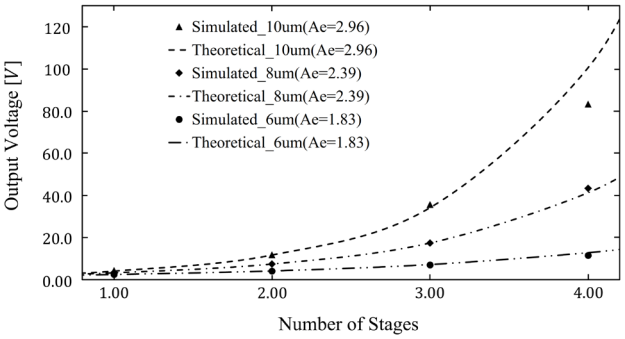


**Fig. 17** Output voltage exponential dependence on the stage-number, with $C_L = 10pF$, $C_p = 0.20pF$, and $C_j0 = 0.21pF$.

In this simulation, the variable capacitor is represented by an equivalent model obtained by curve-fitting the data of Fig. 12. Simscape™ models are used for circuit elements like diodes and fixed capacitors.

In the simulation system, we have neglected the electro-mechanical coupling term of the resonator that induces the energy loss due to the charge transfer. This simplification is justified for small load capacitance cases. In this case, the electrical energy stored at capacitances is far smaller than the mechanical vibration energy. We examine this point in the next section.

The rise time simulation of the three-stage CVCP system is shown in Fig. 14. Owing to the large capacitance ratio, the output voltage becomes larger than $30V$ with only three stages and $1.8V$ supply voltage. The rise time for $30V$ is $18.7ms$ when the load capacitance is $10pF$. The relatively long rise time, compared to DCP, is stemming from the low resonance frequency value of $40.2kHz$ and the small $C_{max}$.

The relationship between gain $A$ and zero-bias junction capacitance $C_{j0}$ for several capacitance ratios $C_{max}/C_{min}$ is shown in Fig. 15. This shows that we can estimate the maximum output voltage and effective resistance based on the constant junction capacitance approximation.

The parasitic capacitance estimation of SOG process is discussed in refs [34], [35]. We have used the same approach to derive the parasitic capacitance $C_p$ and it was found to be $0.20pF$. To account for the estimation error, the $C_p$ dependence is calculated for several $C_{max}/C_{min}$ cases, as plotted in Fig. 16. As can be seen from this result, the CVCP performance is quite sensitive to the parasitic capacitance value. This originates from the $C_p$ dependence of the gain $A$. Thus, minimizing the parasitic capacitance is a key to make an effective CVCP. The employment of SOG process is a practical choice.

The stage number dependence of $V_{max}$, i.e., the output voltage $V_{out}$ when $I_{out}$ is zero, is plotted in Fig. 17. We can confirm that the output voltage will increase exponentially with the stage number $N$. We can also see that the theoretical results are in good agreement with the simulation, except that the output voltage is limited when it exceeds the reverse breakdown voltage of the diodes. Capability of voltage generation above $50V$ is an advantage of CVCP.

Load characteristics of CVCP are shown in Fig. 18. The slight increase of $V_{out}$ at the small output current is caused by the decrease of the diode forward voltage $V_f$ at the small current region. The slope of the voltage-current graph corresponds to the effective resistance $R_{eff}$. The theoretical and simulated values of $R_{eff}$ are shown in Fig. 19. We can confirm good agreement between the theory and simulation.

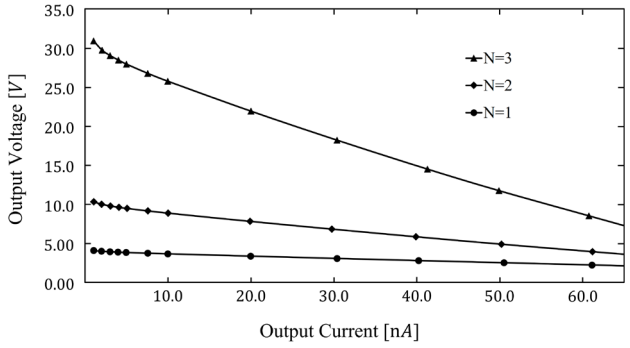


**Fig. 18** Load characteristics of CVCP with $10\mu m$ amplitude, with $C_L = 10pF$, $C_p = 0.20pF$, and $C_j0 = 0.21pF$.

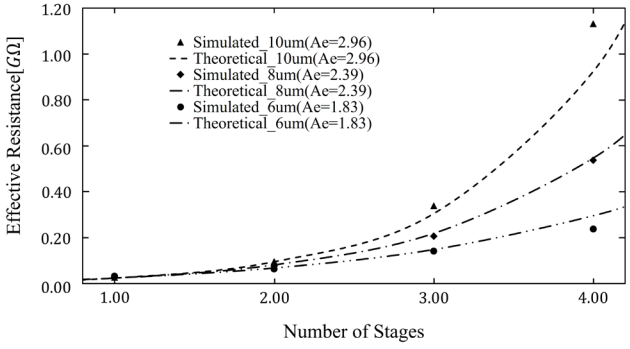


**Fig. 19** Stage number dependence of effective resistance, with $C_L = 10pF$, $C_p = 0.20pF$, and $C_j0 = 0.21pF$.

## 5. Energy Consumption Analysis

The energy consumption of CVCP system has two contributions. First one is the energy supplied from $V_{DD} = 1.8V$. This energy can be calculated from:

$$E_{dd} = \int_0^{t_{rise}} dt V_{DD} I, \tag{24}$$

where $t_{rise}$ is the rise time. Here, we define $t_{rise}$ as the time when the output voltage reaches 95% of the maximum value given by theoretical estimation Eq. (20). Second one is the energy supplied to the resonator. This energy is expressed as

$$E_f = \oint dx F_{drive} = \int_0^{t_{rise}} dt \frac{dx}{dt} F_{drive}. \tag{25}$$

This integration can be carried out explicitly using the steady state solution of $x$ as expressed in Eq. (6). These energies are estimated for several quality factor values, as plotted in Fig. 20. We can see that $E_{dd}$, the energy supplied from $V_{DD}$, is smaller than $E_f$, the energy supplied to the resonator, and is independent of quality factors. The energy $E_f$ becomes smaller for the higher quality factor because less energy is required to sustain the oscillation.

A MEMS CVCP presented here is a combined system

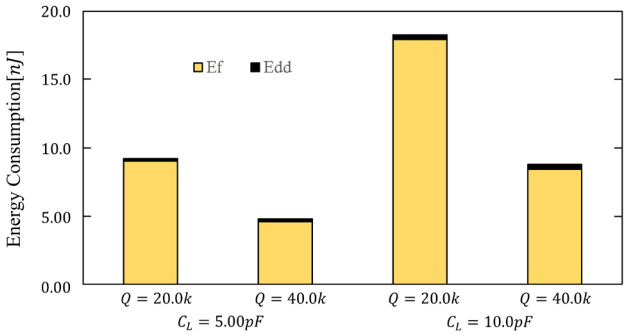


**Fig. 20** Energy consumption of three-stage CVCP when the amplitude is $10\mu m$. Here, $E_f$ is the energy supplied to the resonator, $E_{dd}$ is the energy supplied from the supply voltage $V_{dd}$, and $Q$ is the quality factor of the resonator.

of mechanical and electrical elements. To understand energy consumption, it also is meaningful to grasp the typical energies of the two elements. The vibration energy stored at the ten resonators is

$$E_{vib} = \frac{1}{2} k_{eff} x_0^2 = 48.9nJ, \tag{26}$$

where $k_{eff}$ is the effective spring constant given in Table 2 and $x_0 = 10\mu m$ is the amplitude. On the other hand, the energy stored at the output capacitance when $C_L = 10pF$ and $V_{out} = 30V$ is

$$E_c = \frac{1}{2} C_L V_{out}^2 = 4.50nJ. \tag{27}$$

Thus, the mechanical vibration energy is about 10 times larger than the electrical energy stored at the capacitance.

To explicitly observe the effect of the electro-mechanical coupling term, we have carried out simulations of a single-stage case with a variable capacitance $C(x)$ as in Fig. 12. In this case, the electro-mechanical coupling force has a form

$$F_{coup} = -\frac{d}{dx}\left(\frac{q^2}{2C(x)}\right) \tag{28}$$

with $q$ being a charge stored at $C(x)$. This force can be calculated explicitly, and the amplitude decrease caused by the charge transfer can be monitored. To represent the result, we introduce an amplitude attenuation ratio defined by

$$R_a = \frac{x_0 - x_{rise}}{x_0}, \tag{29}$$

where $x_0 = 10\mu m$ is the initial amplitude and $x_{rise}$ is the amplitude at the rise time $t_{rise}$. The simulations were carried out with no external force, which means that the amplitude decrease is purely due to the charge transfer. Other parameters are the same as in Table 2. The result is plotted in Fig. 21. We can see that the amplitude decrease is negligible ($< 0.50\%$) when the load capacitance $C_L$ is small enough ($< 10pF$). This result shows the legitimacy of our multi-stage simulation results.

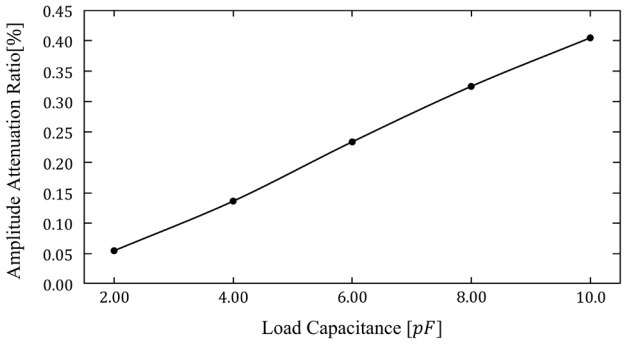


**Fig. 21** Load capacitance dependence of the amplitude attenuation ratio $R_a$ simulated for single-stage.

## 6. Conclusion

A novel charge pump that attains the charge transfer by a variable capacitor has been proposed. Thanks to the excellent charge transfer capability of the anti-phase drive scheme, the multi-stage version enables output voltage exponentially dependent on the stage number. The operating principle of CVCP resembles that of peristaltic pumps. In the MEMS version of CVCP, the capacitance change is brought about by a high-$Q$ MEMS resonator. The results of steady-state analytical model are in good agreement with the simulation results. The three-stage MEMS CVCP is shown to produce a voltage higher than $30V$, owing to the large capacitance difference between the maximum and minimum capacitance states.

This charge pump can be used for devices that require high voltage generation in the MEMS layer. Especially, the MEMS CVCP is suited for supply voltage generation of vibration energy harvesting systems. This application seems attractive since the environmental vibrational energy can be directly utilized to drive the MEMS resonator. The circuit area of our MEMS CVCP, $4.2mm^2$, is not a small value as a charge pump. But it is far smaller than the typical chip size of a vibrational energy harvester (VEH). For example, a chip size is $600mm^2$ for a MEMS VEH of Toshiyoshi et al. [36]. In the future, we plan to survey a CVCP architecture suited for VEH applications.

## Acknowledgments

This work is partly supported by Kioxia corporation. The authors would like to appreciate R. Ito and R. Fujimoto of Kioxia corporation for their helpful comments. The authors are also grateful to H. Maekoba and A. Parent for support on FEM simulations. This work was supported through the activities of VDEC, The University of Tokyo, in collaboration with NIHON SYNOPSYS G.K. Menghan Song is sponsored by the China Scholarship Council.

### References

[1] T. Tanzawa, T. Tanaka, K. Takeuchi, and H. Nakamura, "Circuit techniques for a 1.8-V-only NAND flash memory," IEEE J. Solid-State Circuits, vol.37, no.1, pp.84–89, Jan. 2002.

[2] T. Ying, W.-H. Ki, and M. Chan, "Area-efficient CMOS charge pumps for LCD drivers," IEEE J. Solid-State Circuits, vol.38, no.10, pp.1721–1725, Oct. 2003, doi: 10.1109/JSSC.2003.817596.

[3] J. Che, C. Zhang, Z. Liu, Z. Wang, and Z. Wang, "Ultra-low-voltage low-power charge pump for solar energy harvesting systems," 2009 International Conference on Communications, Circuits and Systems, pp.674–677, July 2009, doi: 10.1109/ICCCAS.2009.5250409.

[4] X. Liu, L. Huang, K. Ravichandran, and E. Sánchez-Sinencio, "A highly efficient reconfigurable charge pump energy harvester with wide harvesting range and two-dimensional MPPT for Internet of Things," IEEE J. Solid-State Circuits, vol.51, no.5, pp.1302–1312, May 2016, doi: 10.1109/JSSC.2016.2525822.

[5] H. Kawauchi and T. Tanzawa, "A 2V 3.8μW fully-integrated clocked AC-DC charge pump with 0.5V 500Ω vibration energy harvester," 2019 IEEE Asia Pacific Conference on Circuits and Systems (APCCAS), pp.329–332, 2019.

[6] M. Innocent, P. Wambacq, S. Donnay, W. Sansen, and H. De Man, "A linear high voltage charge pump for MEMs applications in 0.18μm CMOS technology," ESSCIRC 2004-29th European Solid-State Circuits Conference (IEEE Cat. no.03EX705), pp.457–460, Sept. 2003, doi: 10.1109/ESSCIRC.2003.1257171.

[7] D.S. Hong and M.N. El-Gamal, "Low operating voltage and short settling time CMOS charge pump for MEMS applications," Proc. 2003 International Symposium on Circuits and Systems, 2003. ISCAS '03., vol.5, pp.V–V, May 2003.

[8] A.H. Alameh and F. Nabki, "A 0.13-μm CMOS dynamically reconfigurable charge pump for electrostatic MEMS actuation," IEEE Transactions on Very Large Scale Integration (VLSI) Systems, vol.25, no.4, pp.1261–1270, 2017.

[9] X. Li, R. Li, C. Ju, B. Hou, Q. Wei, B. Zhou, Z. Chen, and R. Zhang, "A regulated temperature-insensitive high-voltage charge pump in standard CMOS process for micromachined gyroscopes," Sensors, vol.19, no.19, p.4149, Sept. 2019.

[10] J.F. Dickson, "On-chip high-voltage generation in MNOS integrated circuits using an improved voltage multiplier technique," IEEE J. Solid-State Circuits, vol.11, no.3, pp.374–378, 1976, doi: 10.1109/JSSC.1976.1050739.

[11] T. Tanzawa and T. Tanaka, "A dynamic analysis of the Dickson charge pump circuit," IEEE J. Solid-State Circuits, vol.32, no.8, pp.1231–1240, Aug. 1997, doi: 10.1109/4.604079.

[12] S. D'Arrigo, G. Imondi, G. Santin, M. Gill, R. Cleavelin, S. Spagliccia, E. Tomassetti, S. Lin, A. Nguyen, P. Shah, G. Savarese, and D. McElroy, "A 5 V-only 256 kbit CMOS flash EEPROM," Proc. 1989 International Symposium on Circuits and Systems, 1989, pp.132–133, Feb. 1989.

[13] A. Umezawa, S. Atsumi, M. Kuriyama, H. Banba, K. Imamiya, K. Naruke, S. Yamada, E. Obi, M. Oshikiri, T. Suzuki, and S. Tanaka, "A 5-V-only operation 0.6- mu m flash EEPROM with row decoder scheme in triple-well structure," IEEE J. Solid-State Circuits, vol.27, no.11, pp.1540–1546, Nov. 1992, doi: 10.1109/4.165334.

[14] M.R. Hoque, T. Ahmad, T. McNutt, A. Mantooth, and M.M. Mojarradi, "Design technique of an on-chip, high-voltage charge pump in SOI," 2005 IEEE International Symposium on Circuits and Systems, pp.133–136 vol.1, May 2005.

[15] Y. Okamoto, H. Takehara, K. Fujimoto, T. Ichiki, T. Ohba, and Y. Mita, "On-chip high-voltage charge pump with MEMS post-processed standard 5-V CMOS on SOI for electroosmotic flow micropumps," IEEE Electron Device Lett., vol.39, no.6, pp.851–854, June 2018, doi: 10.1109/LED.2018.2829925.

[16] M.-D. Ker and S.-L. Chen, "Ultra-high-voltage charge pump circuit in low-voltage bulk CMOS processes with polysilicon diodes," IEEE Trans. Circuits Syst. Express Briefs, vol.54, no.1, pp.47–51, Jan. 2007, doi: 10.1109/TCSII.2006.882854.

[17] K.L. Tai, "System-in-package (SIP): challenges and opportunities," Proc. 2000 Asia and South Pacific Design Automation Confer-

ence, Yokohama, Japan, pp.191–196, Jan. 2000, doi: 10.1109/ASP-DAC.2000.835095.
[18] Y. Lin, R. Liu, W.-C. Li, M. Akgul, and C.T.-C. Nguyen, "A micromechanical resonant charge pump," 2013 Transducers & Eurosensors XXVII: The 17th International Conference on Solid-State Sensors, Actuators and Microsystems (TRANSDUCERS & EUROSENSORS XXVII), pp.1727–1730, June 2013.
[19] G. Zhanshe, C. Fucheng, L. Boyu1, C. Le, L. Chao, and S. Ke, "Research development of silicon MEMS gyroscopes: a review," Microsyst. Technol. vol.21, no.10, pp.2053–2066, 2015.
[20] J.T.M. van Beek and R. Puers, "A review of MEMS oscillators for frequency reference and timing applications," Journal of Micromechanics and Microengineering, vol.22, no.1, p.013001, 2012.
[21] L. Gobbi, A. Cabrini, and G. Torelli, "A discussion on exponential-gain charge pump," 2007 18th European Conference on Circuit Theory and Design, 2007, doi: 10.1109/ECCTD.2007.4529671.
[22] L.-K. Chang and C.-H. Hu, "High efficiency MOS charge pumps based on exponential-gain structure with pumping gain increase circuits," IEEE Trans. Power Electron., vol.21, no.3, pp.826–831, May 2006, doi: 10.1109/TPEL.2006.874795.
[23] O.-Y. Wong, H. Wong, W.-S. Tam, and C.-W. Kok, "Topology, analysis, and CMOS implementation of switched-capacitor DC-DC converters," Facta Universitatis, Series: Electronics and Energetics, vol.27, no.1, pp.41–56, March 2014.
[24] C.T.-C. Nguyen and R.T. Howe, "An integrated CMOS micromechanical resonator high-Q oscillator," IEEE J. Solid-State Circuits, vol.34, no.4, pp.440–455, April 1999.
[25] K.R. Cioffi and W.-T. Hsu, "32KHz MEMS-based oscillator for low-power applications," Proc. 2005 IEEE International Frequency Control Symposium and Exposition, 2005, pp.551–558, Aug. 2005, doi: 10.1109/FREQ.2005.1573992.
[26] H.G. Barrow, T.L. Naing, R.A. Schneider, T.O. Rocheleau, V. Yeh, Z. Ren, and C.T.-C. Nguyen, "A real-time 32.768-kHz clock oscillator using a 0.0154-mm$^2$ micromechanical resonator frequency-setting element," 2012 IEEE International Frequency Control Symposium Proceedings, pp.1–6, May 2012.
[27] F.Y. Kuo, C.F. Chang, and K.A. Wen, "CMOS 0.18μm standard process capacitive MEMS high-Q oscillator with ultra low-power TIA readout system," SENSORS, 2014 IEEE, pp.911–914, Nov. 2014, doi: 10.1109/ICSENS.2014.6985149.
[28] M.A. Unger, H.-P. Chou, T. Thorsen, A. Scherer, and S.R. Quake, "Monolithic microfabricated valves and pumps by multilayer soft lithography," Science, vol.288, no.5463, pp.113–116, April 2000, doi: 10.1126/science.288.5463.113.
[29] M.-H. Wu, S.-B. Huang, Z. Cui, Z. Cui, and G.-B. Lee, "Development of perfusion-based micro 3-D cell culture platform and its application for high throughput drug testing," Sens. Actuators B Chem., vol.129, no.1, pp.231–240, Jan. 2008.
[30] C.T.-C. Nguyen, "MEMS technology for timing and frequency control," IEEE Trans. Ultrason. Ferroelectr. Freq. Control, vol.54, no.2, pp.251–270, Feb. 2007, doi: 10.1109/TUFFC.2007.240.
[31] F. Yang, G. Han, J. Yang, M. Zhang, J. Ning, F. Yang, and C. Si, "Research on wafer-level MEMS packaging with Through-Glass Vias," Micromachines (Basel), vol.10, no.1, p.15, Dec. 2018.
[32] M.C. Lee, S.J. Kang, K.D. Jung, S.-H. Choa, and Y.C. Cho, "A high yield rate MEMS gyroscope with a packaged SiOG process," J. Micromech. Microeng., vol.15, no.11, pp.2003–2010, Nov. 2005.
[33] V. Lindroos, M. Tilli, A. Lehto, T. Motook, "Silicon-On Glass MEMS Design Handbook," Michigan, USA, 2007.
[34] P. Dak, A. Ebrahimi, and M.A. Alam, "Non-faradaic impedance characterization of an evaporating droplet for microfluidic and biosensing applications," Lab Chip, vol.14, no.14, pp.2469–2479, July 2014, doi: 10.1039/C4LC00193A.
[35] J. Wei, "Distributed capacitance of planar electrodes in optic and acoustic surface wave devices," IEEE J. Quantum Electron., vol.13, no.4, pp.152–158, April 1977, doi: 10.1109/JQE.1977.1069319.
[36] H. Toshiyoshi, S. Ju, H. Homma, C-H. Ji, and H. Fujita, "MEMS vibrational energy harvesters," Science and Technology of Advanced Materials, vol.20, no.1, pp.124–143, Feb. 2019.

**Menghan Song** received the B.S. degree in Electronic Science & Engineering from Southeast University, Nanjing, China, in 2020, and the M.S. degree in Micro-electromechanical systems from Waseda University Ike. Lab, Fukuoka, Japan, in 2021, where she is currently pursuing her Ph.D. Her research interests include MEMS charge pump and its process fabrication.

**Tamio Ikehashi** received PhD in theoretical physics from University of Tokyo, in 1995. At the same year, he joined circuit design team of Toshiba corporation and was involved in circuit design of flash memories. He starts research and development of MEMS from 2004. Since then, he developed various MEMS devices, including RF-MEMS tunable capacitors, pressure sensors, hydrogen sensors, accelerometers, and gyro sensors. He became an associate professor of Waseda University from April, 2019.